Journal of Molecular Catalysis A: Chemical 335 (2011) 14–23

Contents lists available at ScienceDirect

Journal of Molecular Catalysis A: Chemical

journal homepage: www.elsevier.com/locate/molcata

Editor's choice paper

Size effect in CO oxidation over magnesia-supported ZnO nanoparticles

Olga Z. Didenko, Gulnara R. Kosmambetova, Peter E. Strizhak*

L.V. Pisarzhevsky Institute of Physical Chemistry of the National Academy of Sciences of Ukraine, Prosp. Nauky, 31, Kyiv-28, 03028, Ukraine

ARTICLE INFO

Article history:
Received 29 January 2010
Received in revised form 6 December 2010
Accepted 13 December 2010
Available online 22 December 2010

Keywords:
ZnO
Colloidal technique
Particle size distribution
CO oxidation
Quantum confinement effect

ABSTRACT

The size effect of ZnO nanoparticles on catalytic activity of ZnO/MgO solids was studied in CO oxidation. We have developed a simple method for preparing supported materials containing ZnO nanoparticles of a controllable size with the same chemical composition, structure, and shape. We revealed that the turnover frequency of CO oxidation on ZnO nanoparticles of variable average radius (2.0–2.3 nm) shows bell-shaped dependence on ZnO nanoparticle size. A dependence of catalytic activity of ZnO nanoparticles on their electronic structure is found. This allows us to explain a maximum in the CO oxidation activity observed for ZnO nanoparticles with the size of about 2.2 nm within the framework of the quantum confinement effect.

1. Introduction

High-dispersed particles of the active metals and their oxides in the size range less than 100 nm are of permanent interest due to their potential applications in electronics, luminescent devices, gas sensors, catalysts etc. [1–4]. The size effect in catalysis over metallic nanoclusters is well studied since the Boudart's discovery of structural sensitive and structural insensitive reactions [5]. It has been established that the particle size of supported metallic catalysts may affect their performance in various catalytic reactions [6–11].

There are several explanations for specific catalytic activity of the metallic nanoparticles smaller than 10 nm. The possible factors changing the activity of nanoscale metal-containing catalysts compared to bulk matters are the high surface area, the increase of percentage of atoms at the material surface, the nature of support, the presence of moisture, the charge transfer, and quantum confinement effects [12–18]. Furthermore, in some cases the catalytic activity correlates with the fraction of surface atoms located on the facets, corners, and edges of metal nanoparticles [19,20]. For example, the catalytic activity of Pt nanoparticles of different shapes increases with the number of surface atoms on the corners and edges of the nanoparticles as the following sequence: cubic < spherical or "near spherical" < the tetrahedral structure [19]. It has been long considered that gold was inactive in catalysis. However, nanocrystalline gold supported on different oxides has been found to be most active in redox reactions [12–15]. A number of effects may contribute to the non-monotonic catalytic activity of gold nanoparticles of 2–5 nm [21]. The most important effect is related to the availability of low-coordinated gold atoms on the small particles [21,22]. Also the quantum confinement effect has been proposed to explain the high anomalous activity and selectivity of the catalyst nanoparticles in some reactions possibly due to significant modification of the electronic properties compared to the bulk. For example, the bell-shaped dependence of the Au nanoparticle activity on their sizes in the CO oxidation may be explained by the changes of the electronic properties of the Au clusters, characterized by a band gap of 0.2–0.6 eV [16]. This effect is associated primarily with the metal-to-insulator transition, which occurs as the Au particle size falls below 3.5 nm. Also the bell-shaped activity dependence of alumina-supported Pt nanoparticles on their size (1.3–10 nm) was observed in total methane oxidation [23]. The bell-shaped size dependence is explained by transformation of supported platinum from ionic to metallic form with the particle increasing. The maximum activity is observed for Pt crystallites of ca. 2 nm containing comparable amounts of partially oxidized and metallic platinum species. For catalysts containing predominantly metallic platinum with particle size above 2 nm the size dependence of their catalytic activity is well described by a simple thermodynamic approach. In this case, the catalytic activity decreases with the particle enlargement. If the particle size is less than 2 nm the catalytic activity decreases at the diminishing particle size due to the predominance of the partially oxidized platinum and a strong interaction with support. The changes of the electronic states with increasing size were observed not only for gold and platinum containing cat-

* Corresponding author. Tel.: +380 44 5256663; fax: +380 44 5256663.
E-mail addresses: didenko_oz@yahoo.co.uk (O.Z. Didenko), kosmambetova@yahoo.co.uk (G.R. Kosmambetova), pstrizhak@hotmail.com (P.E. Strizhak).

1381-1169/$ – see front matter © 2010 Elsevier B.V. All rights reserved.
doi:10.1016/j.molcata.2010.12.005

alysts but also for oxide-supported silver and palladium clusters [9,24–26].

A study of the size effects in catalysis over nanosized metal oxides is more complicated because the quantum confinement effect appears in some cases as nanoparticle size decreases [27–32]. The difficulty of preparation and characterization of oxide catalysts with uniform size and shape prevents to distinguish the quantum confinement effect from other size-dependent effects caused by differences not only of the particle size but also of oxide structure, coordination of the edges and corners, and charge transfer between catalyst and support. Generally, the presence of the quantum confinement effect in a nanosized oxide system is identified by the appearance of a shift in the UV–vis absorbance onset or by a widening of the band gap as compared with the bulk material.

There are studies devoted to comparison of catalysts containing commercial or nanocrystalline oxides of several metals: Zn, Cu, and Ni [27]. It was found that nanoparticles ZnO (3.9 nm) and NiO (3.1 nm) were much more active catalysts than the commercially available materials for the catalytic production of methanol from hydrogen and carbon dioxide. The high activity of catalysts containing nanocrystalline oxides is explained by their higher surface areas compared to commercial samples.

ZnO is one of the oxides used as support, active component, promoter and model system in heterogeneous catalysis [33–36]. Furthermore, ZnO is characterized by high value of melting point and could be used as structural and textural modifier of multicomponent solid catalysts [37–39]. On the other hand, zinc oxide is a semiconductor that shows the quantum confinement effect in experimentally accessible size range (<10 nm) caused by the increase of band gap with decreasing particle size [40,41]. Unfortunately the influence of the quantum confinement effect on the properties of ZnO nanoparticles was observed only for photocatalytic reactions [33,42,43].

In this paper the ZnO/MgO solid was chosen as model system for studying the size effect on activity of oxide catalysts. To achieve this goal, we developed a method for the preparation of ZnO/MgO catalysts with controllable size of supported ZnO nanoparticles by changing conditions of the colloidal solution aging (pH, temperature, composition, and time). The developed approach is based on deposition of the zinc oxide nanoparticles from colloidal solution without surfactant on magnesia [44]. MgO is known as suitable support material due to its inertness in different chemical reactions. The use of colloidal technique for the preparation of ZnO/MgO catalysts led to the formation of uniform "near spherical" ZnO nanoparticles.

The morphology of ZnO nanoparticles was investigated by two complementary methods: transmission electron microscopy (TEM) and UV–vis absorption and diffuse reflectance (DR) spectroscopy. Molecular carbon monoxide is one of the most widely used indicators for local surface structure and an ideal probe molecule for investigating the influence of particle size on catalytic properties [36,45]. Thus, the relationship between catalytic activity and size of ZnO nanoparticles was investigated in CO oxidation [36,46,47].

2. Experimental

2.1. Materials

All chemicals and solvent (zinc acetate dihydrate, sodium hydroxide, magnesium oxide, absolute 2-propanol from Ukraine Chemical Reagents Co.) were of the highest purity available and were used as received. CO gas was purified by molecular sieve traps before it was used. Before use the magnesia was calcinated at 500 °C in air for 5 h to remove water and carbonate.

2.2. Catalyst preparation

Magnesia-supported ZnO catalysts were prepared using a two-step procedure: formation of ZnO nanoparticles in a colloidal solution and deposition of ZnO nanoparticles from colloidal solution on MgO.

The preparation of ZnO colloidal solution followed the method of Bahnemann et al. with some modifications [48,49]. Two precursor solutions were prepared by dissolving 0.57 mmol of $Zn(CH_3COO)_2{\cdot}2H_2O$ in 92 mL of 2-propanol and 1.14 mmol of NaOH in 8 mL of 2-propanol under stirring at about 50 °C, after both solutions were cooled to 0 °C. At this temperature the hydroxide solution was added dropwise to the prepared zinc acetate solution under vigorous stirring. The mixture containing 5.7×10^{-3} M zinc acetate and 1.14×10^{-2} M hydroxide was immersed in a water bath preheated to 60 °C for aging. After 2.5 h a transparent colloidal solution of ZnO nanoparticles was obtained. Schematically the overall nucleation reaction is presented as [50,51]:

$$Zn(CH_3COO)_2 + 2NaOH \rightarrow ZnO + 2CH_3COONa + H_2O$$

The synthesis of ZnO/MgO catalyst was carried out by mixing 27 mL of ZnO colloidal solution with 10 mL of suspension containing 1 g MgO powder under constant stirring at temperature ≤4 °C for 15–20 min. The MgO suspension was cooled below 4 °C under vigorous stirring before the ZnO colloid was added. Solid product was separated by filtration, washed several times with 2-propanol and dried in air at 70 °C followed by calcinating in air at 350 °C for 4 h.

A series of ZnO/MgO samples with different sizes of ZnO nanoparticles were prepared by varying the conditions of the colloidal solution aging (temperature, pH, time, and reagent concentration). The value of pH in the ZnO colloidal solution (5.4–7.5) was varied by adding appropriate amount of 0.1 M solution of CH_3COOH in 2-propanol for adjustment. The temperature of ZnO colloid aging was varied within 20–60 °C. The molar ratio of $Zn(CH_3COO)_2$:NaOH was set for preparation of colloidal solution as 1:2 and 1:1.6 with concentration of zinc acetate in the range of 3.4×10^{-3}–1×10^{-2} M.

The amount of colloidal solution and support was calculated as having a final ZnO loading of 1 wt.%.

The catalyst containing bulk ZnO was prepared for comparison purposes by mixing a commercial powder of ZnO (1 wt.%) and MgO in 2-propanol suspension. The drying of the ZnO^{bulk}–MgO catalyst was conducted in air at 70 °C followed by calcination in air at 350 °C for 4 h.

2.3. Characterization techniques

There are different methods for characterization of morphology and structure of nanoparticles in colloidal solutions or solids: transmission electron microscopy (TEM), ultraviolet–visual (UV–vis) absorption or diffuse reflectance (DR) spectroscopy, powder X-ray diffraction (XRD) and others [52]. Generally the combination of several methods and their comparison gives the most correct characteristic about the particles size. Unfortunately, some of these methods cannot be applied for the determination of the particle size in powder samples with low content (<5%) or very small particles (≤2 nm). In this case, the average particle size may be estimated by TEM. However, the accuracy of the size determination of supported ZnO particles by TEM is complicated mainly due to the low contrast resolution between the ZnO particles and the support. DR spectroscopy is an alternative and non-destructive technique to obtain the average size of supported particles in solid composite with minimum sample preparation. Especially this method may be useful to characterize zinc oxide particles. ZnO is one of the

semiconducting oxides whose properties are well studied by spectroscopic methods. The ZnO nanosized particles exhibit an increase in the band gap or a shift in the UV–vis absorbance onset toward shorter wavelengths compared with bulk ZnO which is attributed to the quantum confinement effect. We used both TEM and UV–vis absorption or DR spectroscopy to ensure trustworthy information about morphology of ZnO nanoparticles in colloidal or solid systems.

The structural characteristics of the prepared solids were investigated by an X-ray diffractometer (DRON-3M, Bourevestnik, Inc., USSR) with CuK_α radiation ($\lambda = 0.154$ nm) filtered through Ni.

The morphology of obtained products was characterized by TEM using PEM-125K (Selmi, Ukraine). Samples for TEM measurements were prepared by placing a drop of 2-propanol colloidal solution or ZnO/MgO suspension onto a carbon-coated copper grid and allowing the solvent to evaporate in air. The powder samples of catalysts have been previously ultrasonically dispersed in 2-propanol.

Optical properties and sizes of ZnO nanoparticles in the colloidal solution and supported on MgO were examined by UV–vis absorption and DR spectroscopy using Specord M-40. The UV–vis absorption spectra from colloidal solutions were obtained with 1 cm quartz cells. The UV–vis DR spectra of the ZnO/MgO powder samples were obtained with MgO as a reference. All measurements were carried out at ambient temperature (22 ± 1 °C).

The particle size distribution and the average size of ZnO nanoparticles were estimated from the TEM images by measurement of 300–400 particles and the UV–vis absorption or DR spectroscopy using effective mass approximation. The accuracy of the ZnO nanoparticle average radius was ±0.1 nm by the UV–vis spectroscopy and ±0.05 nm by TEM. The UV–vis DR spectroscopy was also used to evaluate the dispersion of the ZnO particles (D_{ZnO}) as the surface fraction of the total number of ZnO molecules in catalyst.

The content of ZnO in ZnO/MgO was determined by titrimetric analysis and amounted to 0.8–1.2 wt.%.

The surface area of the prepared catalysts was measured by N_2 adsorption at −196 °C using the BET (Brunauer–Emmet–Teller) method. The BET surface area of initial MgO after calcination is $S_{BET} = 13.5\ m^2\ g^{-1}$.

2.4. Catalyst testing

The prepared ZnO/MgO samples were tested in CO oxidation by O_2 using the flow method. The catalyst sample (ca. 1 cm^3) with 1–2 mm mesh particles was loaded in the middle of the quartz flow tube reactor (length 20 cm and 0.9 cm internal diameter) and put between two layers of the granulated quartz glass (0.5 cm^3 on each side). The reactor was placed in a thermoprogrammable vertical electric furnace that allowed maintaining the temperature of the catalyst with an accuracy of less than ±5 °C. The pretreatment of the sample was carried out at 300 °C for 30 min with He under atmospheric pressure followed by cooling to 200 °C. The test gas mixture containing 2 vol.% CO, 20 vol.% O_2 (He as a balance gas) with a flow rate of 100 $cm^3\ min^{-1}$ was used over the temperature range 200–560 °C under atmospheric pressure. The reaction components and product at the reactor outlet (CO, O_2, CO_2) were analyzed on a gas chromatograph. The experiment was repeated several times for each catalyst sample. The experimental precision did not exceed ±5%.

The CO conversion (X) was calculated based on the CO consumption as follows:

$$X(\%) = \frac{[CO]_{in} - [CO]_{out}}{[CO]_{in}} \times 100$$

where $[CO]_{in}$ and $[CO]_{out}$ are the inlet and outlet CO concentration (%), respectively.

The mass-normalized reaction rate was expressed as the number of CO (moles) transformed over mass of catalyst per second as follows:

$$W(mol_{CO}\ s^{-1}\ g_{cat}^{-1}) = \frac{F_{CO}^{in} - F_{CO}^{out}}{W_{cat}}$$

where F_{CO}^{in} and F_{CO}^{out} are the inlet and outlet CO molar flow rates ($mol_{CO}\ s^{-1}$), respectively; W_{cat} is the catalyst weight (g).

The surface-specific activity so-called turnover frequency (TOF, s^{-1}) for CO oxidation was determined as the reaction rate per active site. The TOF value was calculated as the number of the CO molecules reacting per surface-centered ZnO molecules (active sites) in unit time. The number of active sites was obtained using the average radius of the near-spherical ZnO nanoparticle.

3. Results

3.1. Size characterization of ZnO nanoparticles in colloid and solid

As shown in Fig. 1a the TEM image of the ZnO colloid reveals that the nanoparticles are almost spherical. The ZnO nanoparticles size distribution is rather narrow. Approximately 90% of nanoparticles have radius within 1.6–2.4 nm. The average radius of ZnO nanoparticles obtained from the TEM images was evaluated as the simple average value ($\langle r_T \rangle$). In colloidal solution, the $\langle r_T \rangle = 2.0$ nm with standard deviation $\sigma = 0.3$ nm. The absorbance spectrum for ZnO colloid is shown in Fig. 1b. The absorbance onset blue shifted compared with the macrocrystalline ZnO for which the absorbance onset is about 388 nm corresponding to the value of band gap 3.2 eV at room temperature [53]. The absorption edge obtained from the extrapolation of the steep part of the absorption spectrum of the ZnO colloid was calculated as $\lambda_c \approx 365$ nm. The band gap determined as $1240/\lambda_c$(nm) is about 3.4 eV. The widening of the band gap indicates that ZnO nanoparticles in colloidal solution are in the quantum confinement region, i.e. the ZnO nanoparticle radii are smaller than 5 nm, which is in good agreement with TEM.

The ZnO nanoparticle radius was determined from UV–vis spectrum using the effective mass model [50,54]:

$$E^*(r) - E_g^{bulk} = \frac{\hbar^2\pi^2}{2er^2}\left(\frac{1}{m_e^*} + \frac{1}{m_h^*}\right) - \frac{1.8\,e}{4\pi\varepsilon\varepsilon_0 r} - \frac{0.124\,e^3}{\hbar^2(4\pi\varepsilon\varepsilon_0)^2}\left(\frac{1}{m_e^*} + \frac{1}{m_h^*}\right)^{-1},$$

where E^* is the exciton energy in the spherical nanoparticle (eV) with a radius of r (m); E_g^{bulk} is the bulk band gap; $\hbar$ is reduced Planck's constant ($\hbar = h/2\pi = 1.055 \times 10^{-34}$ J s); m_e^* and m_h^* are the effective masses of the electron and hole, respectively (for ZnO $m_e^* = 0.26\,m_e$, $m_h^* = 0.59\,m_e$); m_e is the free electron mass (9.11×10^{-31} kg); e is the charge on the electron (1.602×10^{-19} J/eV); ε is the relative permittivity (for ZnO –8.5); ε_0 is the permittivity of free space (8.854×10^{-12} F/m).

Determination of the particle size distribution from the absorption onset of ZnO nanoparticles is based on the dependence of the optical absorption (A) on the number (N) and radii (r) of the particles by a law of the form $A \propto Nr^3$ [55]. The particle size distribution for ZnO nanoparticles in colloidal solution is obtained as follows [56]:

$$A(r) \propto \int_r^\infty \frac{4}{3}\pi r^3 n(r)\mathrm{d}r,$$

where A is the optical absorption, r is the particle radius, $n(r)$ is the particle size distribution. This statement is valid for diluted solution as long as the particles are spherical and the absorption coefficient

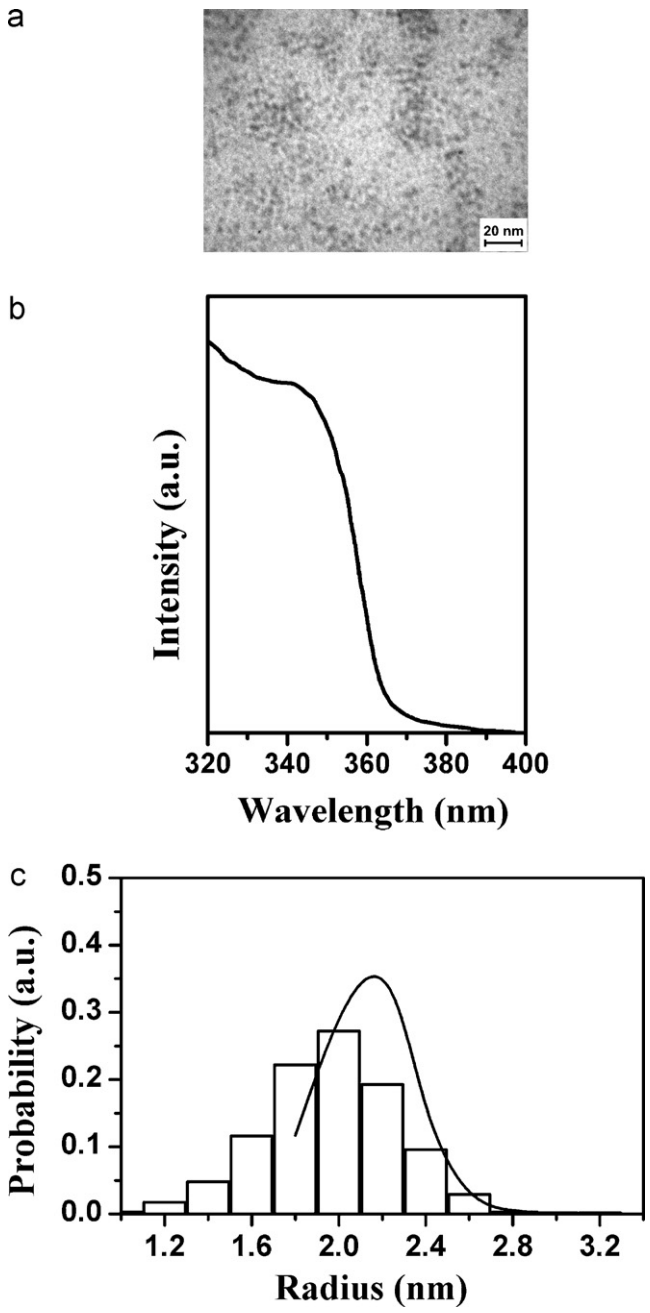

Fig. 1. TEM image (a), absorption spectrum (b), and size distributions of ZnO nanoparticles from the aged colloidal solution diluted at 5 times (c) obtained from TEM image (histogram) and absorption spectrum (solid curve). Conditions of the ZnO colloidal solution preparation: $[Zn(CH_3COO)_2] = 5.7 \times 10^{-3}$ M; $[NaOH] = 1.14 \times 10^{-2}$ M; temperature for aging is 60 °C; aging time is 2.5 h.

is independent of the particle size. After differentiation on radius and noting that $n(r) = 0$ when $r \to \infty$, the expression relating the particle size distribution to the local slope of the absorbance spectrum:

$$n(r) \propto -\frac{dA/dr}{4/3\pi r^3}$$

A comparison of the particle size distributions obtained from the analysis of the TEM image and the absorbance spectrum of the ZnO colloid is presented in Fig. 1c as histogram and solid curve, respectively. A good agreement between the data obtained by both methods is observed. The average radius of ZnO nanoparticles was calculated as number average size using the following

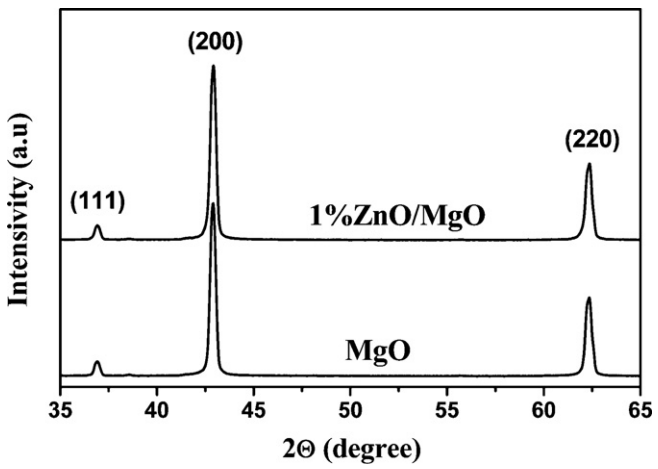

Fig. 2. XRD patterns for pure MgO and 1% ZnO/MgO prepared by deposition of ZnO nanoparticles from colloidal solution on magnesia. Conditions of the ZnO colloidal solution preparation are the same as in Fig. 1.

formula: $\langle r_s \rangle = \Sigma n(r_i) r_i / \Sigma n(r_i)$ where $n(r_i)$ is the number of particles with radius r_i. The ZnO nanoparticles in colloidal solution have an average radius $\langle r_s \rangle = 2.12$ nm with a size distribution of about 97% in the 1.8–2.4 nm range ($\sigma = 0.2$ nm). This value of $\langle r_s \rangle$ corresponds to the average particle radius obtained from the TEM images ($\langle r_T \rangle = 2.0$ nm). Similar results have been observed for the colloidal ZnO nanoparticles synthesized using the same procedure and reported in literature [56].

Fig. 2 shows a typical XRD pattern of the ZnO/MgO solid. The XRD pattern of the initial magnesia is also included in Fig. 2. The sharp diffraction peaks at $2\theta = 36.9$, 42.9, and 62.4 on both spectra are ascribed to MgO (JCPDS 45-0946). The peaks corresponding to the ZnO nanoparticles are not observed in the XRD pattern of ZnO/MgO solid due to the small ZnO concentration.

Fig. 3 shows the TEM image, diffuse reflectance UV–vis spectrum of the ZnO/MgO solid and the corresponding particle size distributions. TEM observation reveals that the ZnO nanoparticles are almost homogeneously dispersed on the surface of the support as illustrated in Fig. 3a and in the inset. The shape of the MgO particles is cubic with sizes in the range of 20–100 nm. The average radius of supported ZnO nanoparticles is $\langle r_T \rangle = 2.2$ nm ($\sigma = 0.3$ nm). For the 1% ZnO/MgO powder, as for any dilute solid systems, superficial reflection is neglected, which is always superimposed upon the diffuse reflection and which therefore distorts the spectrum [57,58]. The scattering phenomena is minimized due to high content of magnesium oxide (99%) also used as reference material. As shown in Fig. 3b the absorption edge in the DR spectrum of the ZnO/MgO solid is blue shifted in comparison with bulk ZnO to 378 nm corresponding to a band gap of about 3.3 eV. The band gap of the bulk ZnO in the ZnO^{bulk}–MgO powder is 3.19 eV, which does not differ significantly from the value of 3.2 eV reported in the literature [53]. Thus, the size of ZnO nanoparticles after their deposition on MgO from colloid remains in the quantum confinement region.

The particle size distribution in the ZnO/MgO solid was obtained from the DR spectrum in a similar way as analysis of absorbance spectrum of colloidal solution. The normalized function of the particles size distribution obtained from analysis of the DR spectra and the TEM images of the ZnO/MgO solid are presented in Fig. 3c as solid curve and histogram, respectively. Similar to results obtained for colloidal solution the distributions predicted by both methods for the ZnO/MgO solid are well correlated. The main part (about 90%) of the ZnO nanoparticle radii are in the 1.8–2.6 nm range. The average ZnO nanoparticle radius determined from analysis of the UV–vis DR spectrum of solid is 2.26 nm ($\sigma = 0.3$ nm) which is in

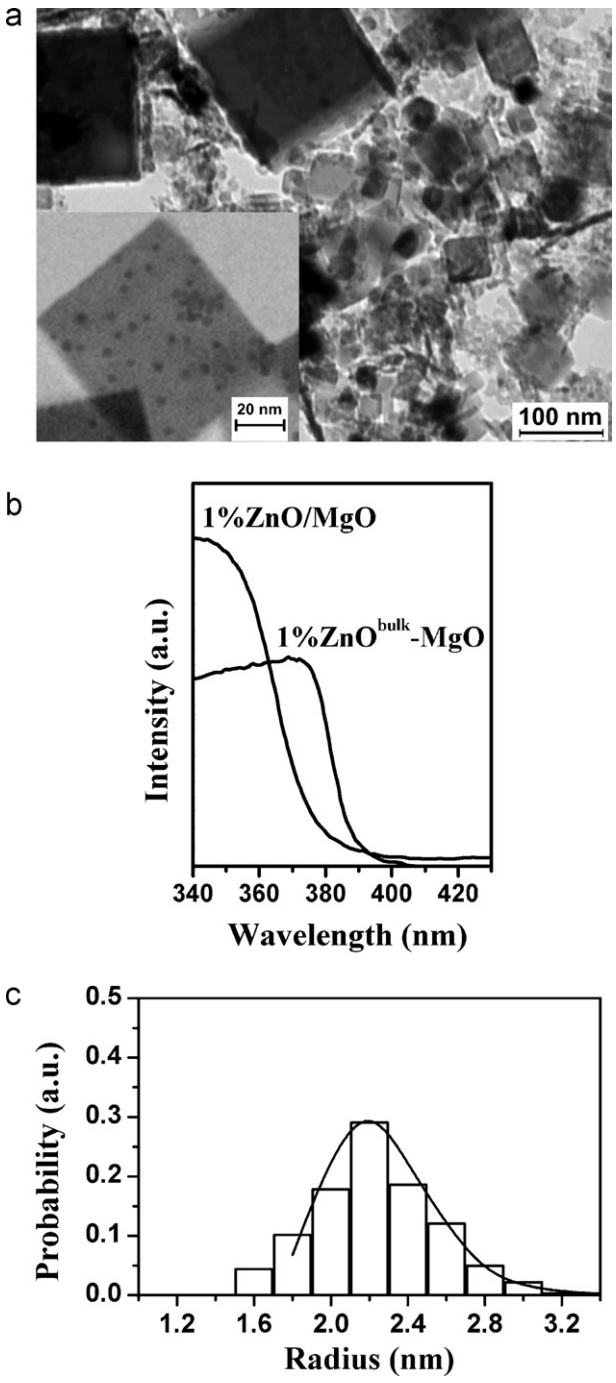

Fig. 3. TEM images (a), diffuse reflectance (DR) spectrum (b), and size distributions of ZnO nanoparticles in the 1% ZnO/MgO solid (c) obtained from TEM images (histogram) and absorption spectrum (solid curve). Conditions of the ZnO colloidal solution preparation are the same as in Fig. 1. For comparison the DR spectrum of the 1% ZnO^{bulk}–MgO powder prepared by mixing of MgO with bulk zinc oxide is given in Fig. 3(b) also.

a good agreement with the average nanoparticle radius obtained from TEM images ($\langle r_T \rangle = 2.2$ nm).

It should be noted that the most probable value of the ZnO nanoparticle radius obtained from TEM and UV–vis spectroscopy is about 2.2 nm both in colloidal solution and in the ZnO/MgO solid. However, the most probable radius of ZnO nanoparticles in colloidal solution obtained from TEM is slightly smaller and equals to 2.0 nm.

Thus, the results obtained from analysis of the TEM images and the UV–vis absorbance spectra for the ZnO colloidal solution and the ZnO/MgO solid are in a good agreement. This demonstrates a possibility to determine the particle size distribution using the UV–vis absorbance spectrum not only for the ZnO colloidal solution but also for the ZnO/MgO solids.

3.2. Effect of the preparation conditions on ZnO nanoparticle size in solid

The ZnO/MgO solids containing ZnO nanoparticles of different size were prepared by varying the conditions of the colloidal solution aging (temperature, pH, time, and reagent concentration). Fig. 4 shows the correlation between conditions of colloid preparation and size of ZnO nanoparticles supported on magnesia. Most of the growth of the colloidal ZnO nanoparticles occurs in the first 40 min after which the particle size does not vary as shown in Fig. 4a.

The influence of pH was studied using colloidal solutions aged of 20 min before mixing with the support. An increase of pH value of colloidal solution within 5.4–7.5 leads to the increase of the average ZnO nanoparticle radius in solid from 1.97 nm up to 2.24 nm as shown in Fig. 4b.

The dependence of the ZnO nanoparticle size in solid on the concentration of zinc acetate in colloidal solutions aged for 10 min passes through a minimum as it follows from the data presented in Fig. 4c. The magnesia-supported ZnO nanoparticles have minimal size at $Zn(CH_3COO)_2$ concentration about 4.8×10^{-3} M. The increase of $Zn(CH_3COO)_2$ concentration within $(4.8–5.7) \times 10^{-3}$ M leads to significant growth of the ZnO nanoparticles in solid, up to 2.23 nm in radius. If the concentration of zinc acetate is above 5.7×10^{-3} M the size of ZnO nanoparticles changes slightly. The largest ZnO nanoparticles ($\langle r_S \rangle = 2.27$ nm) are formed at the minimal concentration of zinc acetate (3.4×10^{-3} M). Probably, this concentration of acetate–ion is not enough for the stabilization of the ZnO colloidal nanoparticles [49]. An increase of pH value in the reaction mixture causes the agglomeration of the unstable ZnO nanoparticles after adding the basic magnesium oxide to the colloidal solution. The buffering capacity of acetate is too small to keep the pH value constant.

The dependence of the average ZnO nanoparticle radius in solid on the aging temperature of the colloidal solution is given in Fig. 4d. The ZnO colloidal nanoparticles grew during 15 min. The average radius of the ZnO nanoparticles supported on magnesia increases slightly in the range of 2.18–2.26 nm as the aging temperature increases from 20 to 50 °C. The sharp decrease of the average ZnO nanoparticles radius down to 2.05 nm is observed at aging temperature of 60 °C. Keeping the solution at the aging temperature of 60 °C for 15 min is sufficient for the formation of stable colloidal ZnO nanoparticles which do not change their size significantly after deposition on magnesia.

It should be noted that the range of ZnO nanoparticle sizes in the ZnO/MgO solid is narrower compared with their colloidal solution if preparation conditions are varied [49,50,56]. This may be caused by an increase of pH value after adding magnesia to the colloidal solution.

3.3. Textural characteristics of ZnO/MgO solids

The textural characteristics of the prepared ZnO/MgO solids were studied by N_2 adsorption and UV–vis DR spectroscopy. The results are given in Table 1. The surface area of the ZnO/MgO samples varies within 9–15 $m^2\,g^{-1}$. The surface area of the 1% ZnO^{bulk}–MgO catalyst containing bulk ZnO is 13 $m^2\,g^{-1}$. The average radius and dispersion of ZnO nanoparticles in the catalyst were calculated from the particle size distribution obtained using the UV–vis DR spectroscopy. They were found to be in the range of 2.01–2.29 nm and 54–62%, respectively.

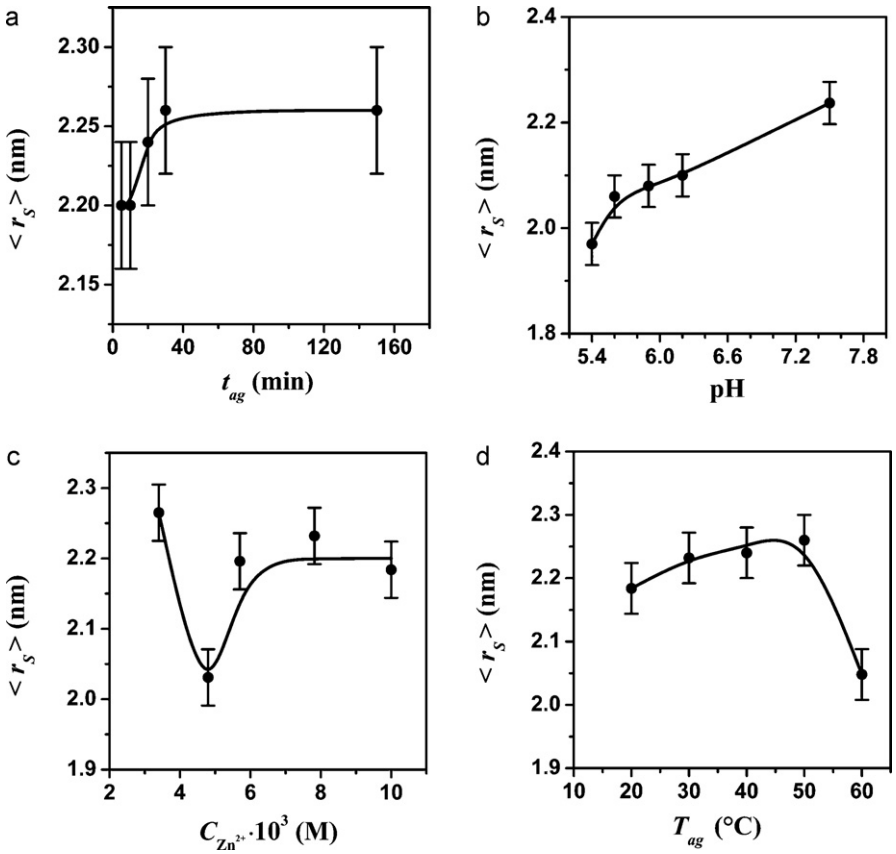

Fig. 4. The influence of aging conditions of the ZnO colloidal solution on size of ZnO nanoparticles supported on magnesia: (a) aging time, t_{ag} ([$Zn(CH_3COO)_2$] = 5.7×10^{-3} M; [NaOH] = 1.14×10^{-2} M; aging temperature T_{ag} = 60 °C); (b) pH of reaction mixture ([$Zn(CH_3COO)_2$] = 5.7×10^{-3} M; [NaOH] = 1.14×10^{-2} M; T_{ag} = 60 °C; t_{ag} = 20 min); (c) concentration of $Zn(CH_3COO)_2$ in reaction mixture ([$Zn(CH_3COO)_2$]:[NaOH] = 1:1.6; T_{ag} = 60 °C; t_{ag} = 10 min); (d) aging tempezature, T_{ag} ([$Zn(CH_3COO)_2$] = 5.7×10^{-3} M; [NaOH] = 1.14×10^{-2} M; t_{ag} = 15 min).

3.4. Catalytic activity of ZnO/MgO solids in CO oxidation

The catalytic activity of the ZnO/MgO samples prepared at different conditions was evaluated for the CO oxidation by O_2 in the temperature range of 200–560 °C. Fig. 5 shows typical plots of the CO conversion as a function of temperature for the ZnO containing catalysts. The plots of the CO conversion versus temperature for all ZnO/MgO have complicated forms. The CO conversion increases stepwise as indicated by two shoulders on each plot. The CO conversion goes up slightly for all ZnO/MgO catalysts; then the first plateau is observed within 220–260 °C for catalyst Cat-6 containing ZnO nanoparticles of average radius $\langle r_S \rangle$ = 2.20 nm, 320–360 °C for Cat-2 ($\langle r_S \rangle$ = 2.03 nm), and 280–420 °C for Cat-10 ($\langle r_S \rangle$ = 2.29 nm). Further rise in temperature leads to steep increase in CO conversion for Cat-2 and Cat-6. For Cat-10 the CO conversion increases only slightly. Afterward, a second plateau is observed in the range of 320–520 °C, 460–520 °C, and 440–480 °C for Cat-6, Cat-2, and Cat-10, respectively, followed by the CO conversion increases again. The maximum value of the CO conversion reaches only 50% for Cat-6 and about 100% for Cat-2 at 560 °C. For Cat-10 the CO conversion rises up to about 55% at 540 °C. Thus the cata-

Table 1
Textural characteristics of the 1% ZnO/MgO catalysts (Cat) and mixture of 1% bulk ZnO with MgO powder.

Catalyst	$\langle r_S \rangle$[a] ± 0.05 (nm)	σ[b] (nm)	S_{BET}[c] ($m^2\ g^{-1}$)	D_{ZnO}[a] (%)
Cat-1	2.01	0.21	14	62
Cat-2	2.03	0.21	14	61
Cat-3	2.05	0.23	12	60
Cat-4	2.12	0.23	12	59
Cat-5	2.16	0.26	11	55
Cat-6	2.20	0.27	10	56
Cat-7	2.23	0.27	9	55
Cat-8	2.25	0.22	10	55
Cat-9	2.26	0.29	15	54
Cat-10	2.29	0.29	15	54
1% ZnO^{bulk}–MgO	–	–	13	–

[a] The average radius and dispersion of ZnO nanoparticles in the 1% ZnO/MgO catalysts calculated from the particle size distribution using the UV–vis DR spectroscopy.
[b] Standard deviation of the average radius.
[c] BET surface area.

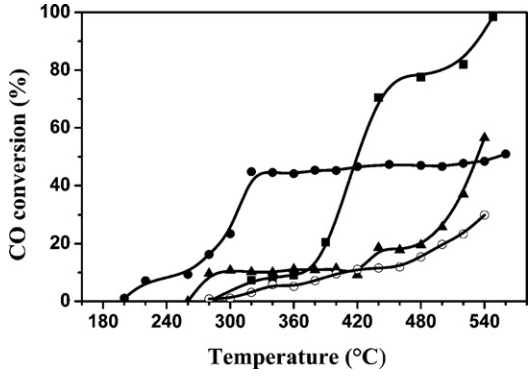

Fig. 5. Comparison of the CO conversion vs. temperature for the 1% ZnO/MgO catalysts containing ZnO nanoparticles of different average radius: (■) 2.03 nm (Cat-2), (●) 2.20 nm (Cat-6), (▲) 2.29 nm (Cat-10), and (○) the 1% ZnO^{bulk}–MgO catalyst containing bulk zinc oxide. Reaction conditions: 2 vol.% CO, 20 vol.% O_2 in He with a total volumetric flow rate of 100 $cm^3\ min^{-1}$.

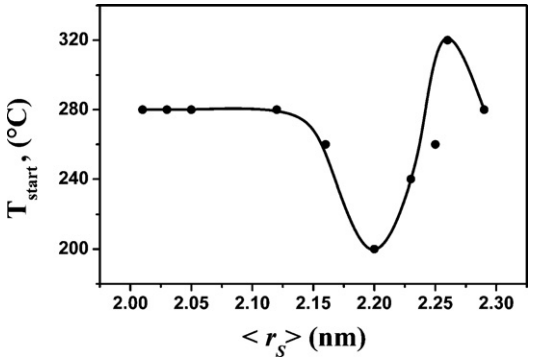

Fig. 6. The start temperature of CO oxidation (T_{start}) as a function of the average radius of ZnO nanoparticles in the 1% ZnO/MgO solids and the 1% ZnO^{bulk}–MgO powder containing bulk zinc oxide. Reaction conditions are the same as in Fig. 5.

lyst Cat-6 containing ZnO nanoparticles with the average radius of $\langle r_S \rangle$ = 2.20 nm exhibits significantly higher activity compared with other ZnO/MgO nanosolids at temperatures 200–400 °C. The lowest activity in CO oxidation is observed for the catalyst containing bulk ZnO for which an increase of the reaction temperature above 310 °C is accompanied by slow rise of the CO conversion up to about 30% at 540 °C.

The structure change of the catalyst surface during reaction may be one of the reasons for the complicated dependence of CO conversion on temperature. At the start of reaction, the CO oxidation occurs on the ZnO nanoparticles leading to the CO_2 formation. Then magnesium carbonate can be formed over the catalyst surface as a result of CO_2 reaction by magnesium oxide. The superficial magnesium carbonate complicates access of reagents (CO and O_2) to active sites of ZnO nanoparticles. Decomposition of the magnesium carbonate at temperatures above 350 °C leads to the steep rise in the catalyst activity. Further temperature increase can cause structural changes of the catalyst surface affecting the catalytic activity of ZnO nanoparticles.

The start temperature of CO oxidation (T_{start}) and the temperature required for 30% and 50% CO conversion ($T_{30\%}$, $T_{50\%}$) were used for comparison of the catalytic activity of prepared samples containing the ZnO nanoparticles of different size and bulk ZnO. A plot of the start temperature of CO oxidation versus the average ZnO nanoparticles radius for ZnO/MgO nanosolids is presented in Fig. 6. The Cat-6 ($\langle r_S \rangle$ = 2.20 nm) is characterized by the minimum temperature values of reaction start (200 °C). For catalysts containing ZnO nanoparticles with average radius 2.16, 2.23, 2.25 nm (Cat-6, Cat-7, Cat-8, respectively), the start temperature of CO oxidation is in the narrow range of 240–260 °C. The maximum value of T_{start} is observed for Cat-9 ($\langle r_S \rangle$ = 2.26 nm) – 320 °C. T_{start} for other catalysts is size-independent and equals 280 °C.

Table 2 gives values of the temperature required for 30% and 50% CO conversion. The minimum temperature value of 30% CO conversion (305 °C) is for Cat-6. However, the temperature required for 50% CO conversion for Cat-6 is 550 °C. This is the maximum value for all studied ZnO/MgO catalysts. Such complicated behaviour of

Table 2
The activity in CO oxidation of the 1% ZnO/MgO catalysts (Cat) and mixture of 1% bulk ZnO with MgO powder[a].

Catalyst	$\langle r_S \rangle$[b] ± 0.05 (nm)	$T_{30\%}$[c] (C)	$T_{50\%}$[c] (°C)	X_{320}[d] (%)
Cat-1	2.01	350	400	7.3
Cat-2	2.03	400	420	7.3
Cat-3	2.05	380	400	7.7
Cat-4	2.12	400	530	8.0
Cat-5	2.16	360	540	24.0
Cat-6	2.20	305	550	44.5
Cat-7	2.23	445	535	16.2
Cat-8	2.25	440	500	12.0
Cat-9	2.26	500	540	6.1
Cat-10	2.29	505	530	10.2
1% ZnO^{bulk}–MgO	–	540 (<30%)	–	3.1

[a] Reactant gas mixture: 2 vol.% CO, 20 vol.% O_2 in He; a total volumetric flow rate = 100 cm^3 min^{-1}.
[b] The average radius of ZnO nanoparticles in the 1% ZnO/MgO catalysts obtained from the UV–vis DR spectrum.
[c] Temperature required for the 30% and 50% CO conversion.
[d] The CO conversion at 320 °C.

catalyst Cat-6 may be caused by the fact that the average size of ZnO nanoparticles affects the activity of ZnO/MgO solids only at temperatures below 350 °C (calcination temperature of the catalyst preparation). At temperature above 350 °C, the catalyst activity is basically influenced by reorganization of the catalyst surface structure. Therefore a temperature below 350 °C, namely 320 °C, was selected for comparison of the catalytic activity of ZnO nanoparticles with different average radius. Furthermore, the experiment not presented in this work has shown that CO oxidation on pure magnesia starts at 350 °C. It is thus assumed that the catalyst activity at 320 °C is caused mainly by the zinc oxide nanoparticles. The CO conversion values at 320 °C (X_{320}) for all catalysts are also given in Table 2. The maximum value of the CO conversion (44.8%) was achieved for Cat-6. The catalyst containing bulk ZnO exhibits the lowest activity compared to other catalysts with X_{320} about 3%.

4. Discussion

The simplest scheme of CO oxidation on ZnO can be described as follows [36]:

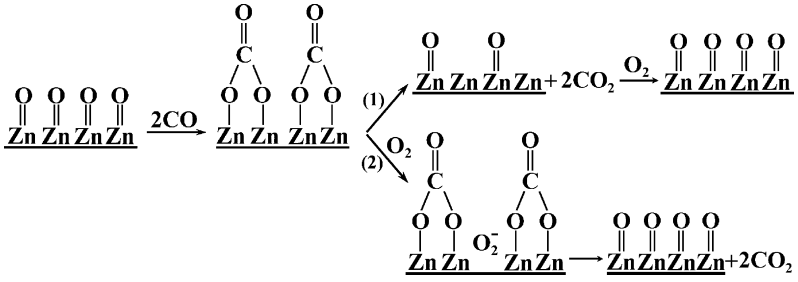

According to the first step, the formation of superficial carbonate structure occurs. Its further decomposition requires considerable activation energy. At high temperature (above 300 °C) the decomposition of the surface carbonate occurs rapidly with formation of CO_2. CO is oxidized according to the stepwise mechanism as presented by reaction (1) in scheme. At low temperature, the decomposition rate of the surface carbonate decreases sharply. The concerted mechanism of the carbonate decomposition and the ZnO reoxidation makes a significant contribution to the process of CO oxidation as presented by reaction (2). Reaction with oxygen adsorbed from the gas there leads to the formation of CO_2. The anions of molecular oxygen formed from adsorbed oxygen are transformed instantly into atomic oxygen anions involved in reaction (2).

As it follows from this mechanism, CO oxidation rate is defined by the quantity of active sites on which oxygen is adsorbed from the

Table 3
The effect of size and exciton energy of the 1% ZnO/MgO catalysts (Cat) on the mass-normalized rate (W) and TOF for CO oxidation at 320 °C[a].

Catalyst	$\langle r_S \rangle$[b] ± 0.05 (nm)	E^*[c] (eV)	W ($\times 10^7$ $mol_{CO} s^{-1} g_{cat}^{-1}$)	TOF ($\times 10^3$ s^{-1})
Cat-1	2.01	3.49	0.8	2.6
Cat-2	2.03	3.48	0.8	2.6
Cat-3	2.05	3.47	0.9	2.6
Cat-4	2.12	3.43	1.1	3.3
Cat-5	2.16	3.40	4.2	9.5
Cat-6	2.20	3.41	10.3	13.1
Cat-7	2.23	3.40	2.2	10.0
Cat-8	2.25	3.42	1.5	9.2
Cat-9	2.26	3.39	0.9	1.5
Cat-10	2.29	3.39	1.5	1.8
1% ZnO^{bulk}–MgO	–	–	0.49	0.7

[a] Reactant gas mixture the same as in Table 2.
[b] The average radius of ZnO nanoparticles in the 1% ZnO/MgO catalysts obtained from the UV–vis DR spectrum.
[c] The exciton energy estimated as $E^* = 1240/\lambda_{1/2}$ ($\lambda_{1/2}$ is the wavelength at which absorption in the UV–vis DR spectrum of the 1% ZnO/MgO solid is 50% of that at the excitonic peak or shoulder).

gas phase. According to the stepwise or concerted reaction mechanism, the active sites are presented by zinc cations and oxygen vacancies on the surface of the catalyst. Both type of active sites are involved in the reaction. With a decrease in the particle size of an active component, the surface-to-volume ratio and number of the oxygen vacancies rapidly increase and the catalytic activity should increase, especially in the case of nanoparticles. The correlation between the oxygen vacancy concentration and ZnO nanoparticle size smaller than 10 nm was experimentally indicated by the appearance of additional peaks in XPS spectra [59].

Furthermore, the differences in the catalytic activity of ZnO nanoparticles for CO oxidation may by caused by structure sensitivity of this reaction. The reaction structure sensitivity may be estimated by the turnover frequency (TOF, s^{-1}), scaling with the inverse nanoparticle size in logarithmic scale [20]. If TOF does not depend on the particle size, reactions are structure-insensitive. Structure-sensitive reactions can be classified into three categories: the TOF increases (a positive particle size effect), decreases (a negative particle size effect), and the TOF passes through a maximum (bell-shaped dependence) with increasing particle size [8,60].

According to the classical structure-sensitivity approach, positive and negative particle size effects are caused by different catalytic activity of active sites localized on the facets, edges or corners of the crystal lattice (geometric factor) [8,56,60,61]. The slope of the linear fit for this scaling characterizes the type of active sites. In general, for structure-sensitive reactions a scaling factor ≥ 1 is obtained, if active sites are localized mainly on the facets; for edges this value is ≥ 2, and for corners it is about 3. For structure-insensitive reactions, the value of the scaling factor is less than 1 [20,61]. The bell-shaped dependence of TOF on particle size is due to changes in the electronic structure of metallic nanocrystallites with size less than 4 nm [8,60]. Similar size dependence of the electronic properties has been observed for Au, Pt, Pd, and Ag supported catalysts [16,23–25].

This may be crucial also for understanding catalytic activity of metal oxide nanoparticles. In fact, details of the near-edge electronic spectra provide useful guidance about intrinsic reaction rates on active transition metal oxide systems. For the first time, the influence of the electronic factor on catalytic activity was reported for highly dispersed metal oxides in oxidative dehydrogenation reactions [29]. The relationship between the catalytic activities for propane oxidative dehydrogenation, the electronic transitions responsible for the UV–vis absorption edge energies, and the surface densities was established for VO_x, MoO_x, WO_x, and NbO_x supported oxides, consisting predominately of two-dimensional domains. For each of these oxides the TOF increases monotonically with decreasing absorption edge energies. Furthermore the lower absorption edge energies correspond to higher metal oxides surface densities characterized for larger particle sizes.

Table 3 shows the correlations between the catalytic activities (mass-normalized reaction rate, W, and surface-specific activity so-called turnover frequency, TOF) of the prepared ZnO/MgO solids and their exciton energies or the average radii of ZnO nanoparticles obtained from the UV–vis DR spectra. The values of W and TOF for CO oxidation were calculated at 320 °C, corresponding to CO conversion less 20% for most of the prepared catalysts. Under such conditions, the CO oxidation rate depends weakly on the concentration of CO and O_2 as the reaction is carried out in kinetic area [60,62]. Besides, the influence of reverse reaction is minimized; therefore observable rate of the CO oxidation is closest to the true value. The exciton energy was estimated as $E^* = 1240/\lambda_{½}$, where $\lambda_{½}$ is the wavelength at which the absorption in the UV–vis DR spectrum of ZnO/MgO solid is 50% of that at the excitonic peak or shoulder [63]. Our results demonstrate that the catalytic activity of the ZnO nanoparticles does not depend on their exciton energy monotonously. The dependence of the catalytic activity on the exciton energy of ZnO nanoparticles has a bell-shaped form as shown in Fig. 7. The catalyst Cat-6 for which the exciton energy is about 3.41 eV ($\langle r_S \rangle = 2.20$ nm) exhibits significantly higher rate compared to samples with smaller and larger exciton energy value (Fig. 7a). A similar correlation between TOF and the exciton energy is observed (Fig. 7b). The highest values of TOF are shown by the catalysts with the exciton energy in a narrow range of 3.40–3.42 eV. These catalysts contain ZnO nanoparticles of average radius of 2.16, 2.20, 2.23, and 2.25 nm (Cat-5, Cat-6, Cat-7, and Cat-8, respectively). It should be noted that the changes of exciton energies and ZnO nanoparticle sizes are not symbate.

The dependence of TOF on the average radius of ZnO nanoparticles is plotted in logarithmic coordinates in Fig. 8. Our experimental results gives a bell-shaped dependence of TOF on ZnO nanoparticle sizes. This plot indicates that the influence of the geometric factor on catalytic activity of ZnO nanoparticles is insignificant compared to the electronic effect.

The correlation between the electronic structure and activity of ZnO nanoparticles may be caused by electronic transitions from the highest occupied molecular orbitals (HOMOs) to the lowest unoccupied molecular orbitals (LUMOs). The electronic structure of ZnO nanoparticles starts to change if its diameter is smaller than 5 nm. This quantum confinement effect is observed as a blue shift in the band gap or exciton energy [49,54].

Fig. 9 demonstrates the dependence of TOF on the average radius of ZnO nanoparticles supported on magnesia. It shows a bell-shaped dependence of TOF on the average radius of ZnO nanoparticles in the solids. The ZnO/MgO solid containing ZnO nanoparticles of average radius about 2.20 nm has maximum activ-

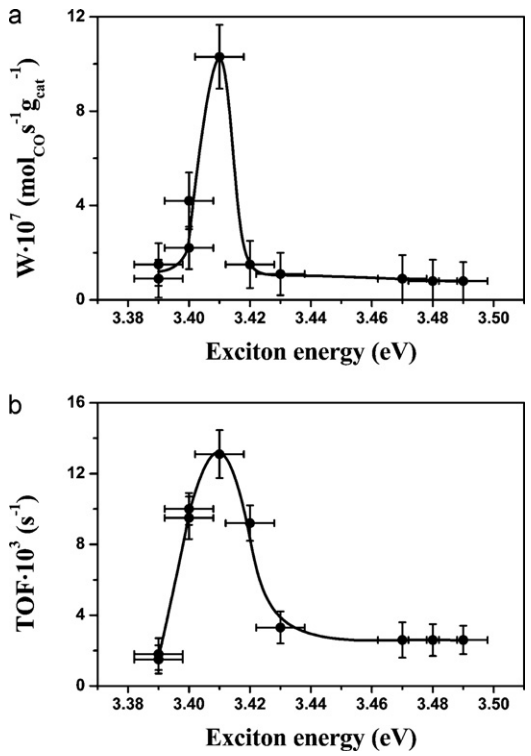

Fig. 7. The mass-normalized rate (a), and turnover frequency (b) of CO oxidation at 320 °C as a function of the exciton energy ($1240/\lambda_{1/2}$) for the 1% ZnO/MgO solids. Other reaction conditions are the same as in Fig. 5.

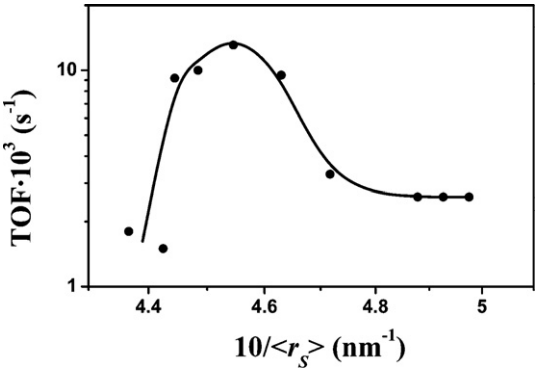

Fig. 8. The turnover frequency of CO oxidation at 320 °C as a function of the inverse average particle radius for the 1% ZnO/MgO solids in logarithmic coordinates. Other reaction conditions are the same as in Fig. 5.

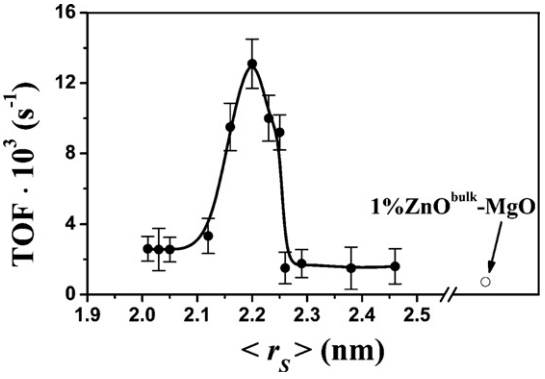

Fig. 9. The turnover frequency of CO oxidation at 320 °C as a function of the average radius of ZnO nanoparticles in the 1% ZnO/MgO solids and the 1% ZnO^{bulk}–MgO powder containing bulk zinc oxide. Other reaction conditions are the same as in Fig. 5.

ity in CO oxidation. It should be noted that the catalysts obtained under different conditions but containing ZnO nanoparticles of the same size exhibit comparable activity for CO oxidation within experimental error. Therefore the bell-shaped dependence of the ZnO/MgO solids activity on the exciton energy and on average radius of ZnO nanoparticles in the range of 2.01–2.29 nm may be caused by quantum confinement effect.

5. Conclusions

Our results show that the catalytic activity of metal oxides nanoparticles may change significantly if their size changes in a relatively narrow range. This has been demonstrated by the dependence of ZnO/MgO solids activity on ZnO nanoparticle sizes in CO oxidation. That has been achieved by developing a relatively simple method for preparing the supported materials containing ZnO nanoparticles of the same chemical composition, structure and shape with varied particle sizes. The developed approach is based on the deposition of preformed zinc oxide nanoparticles of controllable size on magnesia by varying aging conditions of the precursor colloidal solution (time, pH, composition, and temperature).

We found that the TOF for CO oxidation over ZnO nanoparticles having sizes in a narrow range shows a bell-shaped dependence on the exciton energy. It confirms a correlation between the local electronic properties and the catalytic activity of magnesia-supported ZnO nanoparticles. Our results allow explaining the maximum in CO oxidation activity observed for ZnO nanoparticles within the framework of quantum confinement effect. Based on these results we suggest that for some solids, there exists a possibility to predict their catalytic activity based on the UV–vis DR data.

Acknowledgements

This study was supported by funds from scientific research programs of National Academy of Sciences of Ukraine and Ministry of Education and Science of Ukraine.

References

[1] C. Burda, X. Chen, R. Narayanan, M.A. El-Sayed, Chem. Rev. 105 (2005) 1025–1102.
[2] J.P. Wilcoxon, B.L. Abrams, Chem. Soc. Rev. 35 (2006) 1162–1194.
[3] A.P. Weber, M. Seipenbush, G. Kasper, J. Nanopart. Res. 5 (2003) 293–298.
[4] H.H. Kung, M.C. Kung, Catal. Today 97 (2004) 219–224.
[5] M. Boudart, Adv. Catal. 20 (1969) 153–166.
[6] C.R. Henry, Appl. Surf. Sci. 164 (2000) 252–259.
[7] G.C. Bond, Surf. Sci. 156 (1985) 966–981.
[8] M. Che, C.O. Bennett, Adv. Catal. 36 (1989) 55–172.
[9] U. Heiz, W.-D. Schneider, J. Phys. D: Appl. Phys. 33 (2000) R85–R102.
[10] X. Li, D. Ma, X. Bao, Chin. J. Catal. 29 (2008) 259–263.
[11] X. Wang, S.M. Sigmon, J.J. Spivey, H.H. Lamb, Catal. Today 96 (2004) 11–20.
[12] M. Haruta, J. New Mater. Electrochem. Syst. 7 (2004) 163–172.
[13] I.N. Remediakis, N. Lopez, J.K. NØrskov, Appl. Catal. A 291 (2005) 13–20.
[14] L. Guczi, D. Horv th, Z. Pászti, G. Petõ, Catal. Today 72 (2002) 101–105.
[15] G.J. Hutchings, Catal. Today 100 (2005) 55–61.
[16] M.S. Chen, D.W. Goodman, Catal. Today 111 (2006) 22–33.
[17] D.W. Goodman, J. Catal. 216 (2003) 213–222.
[18] S.H. Overbury, V. Schwartz, D.R. Mullins, W. Yan, S. Dai, J. Catal. 241 (2006) 56–65.
[19] R. Narayanan, M.A. El-Sayed, Top. Catal. 47 (2008) 15–21.
[20] M.P. Andersson, F. Abild-Pedersen, I.N. Remediakis, T. Bligaard, G. Jones, J. Engbæk, O. Lytken, S. Horch, J.H. Nielsen, J. Sehested, J.R. Rostrup-Nielsen, J.K. Nrskov, I. Chorkendorff, J. Catal. 255 (2008) 6–19.
[21] N. Lopez, T.V.W. Janssens, B.S. Clausen, Y. Xu, M. Mavrikakis, T. Bligaard, J.K. Nrskov, J. Catal. 223 (2004) 232–235.
[22] M. Turner, V.B. Golovko, O.P.H. Vaughan, P. Abdulkin, A. Berenguer-Murcia, M.S. Tikhov, B.F.G. Johnson, R.M. Lambert, Nature 454 (2008) 981–983.
[23] I.E. Beck, V.I. Bukhtiyarov, I.Yu. Pakharukov, V.I. Zaikovsky, V.V. Kriventsov, V.N. Parmon, J. Catal. 268 (2009) 60–67.
[24] C. Xu, X. Lai, G.W. Zajac, D.W. Goodman, Phys. Rev. B 56 (1997) 13464–13482.
[25] N. Nilius, M. Kulawik, H.P. Rust, H.J. Freund, Surf. Sci. 572 (2004) 347–354.
[26] E.C.H. Sykes, M.S. Tikhov, R.M. Lambert, Catal. Lett. 82 (2002) 169–173.
[27] C.L. Carnes, K.J. Klabunde, J. Mol. Catal. 194 (2003) 227–236.
[28] Y. Jiang, S. Decker, C. Mohs, K.J. Klabunde, J. Catal. 180 (1998) 24–35.

[29] K. Chen, A.T. Bell, E. Iglesia, J. Catal. 209 (2002) 35–42.
[30] P. Li, D.E. Miser, S. Rabiei, R.T. Yadav, M.R. Hajaligol, Appl. Catal. B 43 (2003) 151–162.
[31] K. Nagase, Y. Zheng, Y. Kodama, J. Kakuta, J. Catal. 187 (1999) 123–130.
[32] X. Zheng, S. Wang, S. Zhang, S. Wang, W. Huang, S. Wu, React. Kinet. Catal. Lett. 84 (2005) 29–36.
[33] D. Li, H. Haneda, Chemosphere 51 (2003) 129–137.
[34] N. Homs, J. Llorca1, P.R. de la Piscina, Catal. Today 116 (2006) 361–366.
[35] W. Lu, G. Lu, X. Liu, Y. Guo, J. Wang, Y. Guo, Mater. Chem. Phys. 82 (2003) 120–127.
[36] G.K. Boreskov, Heterogeneous Catalysis, Nova Publishers, New York, 2003.
[37] Y. Liu, Y. Guan, C. Li, J. Lian, G.J. Gan, E.C. Lim, F. Kooli, J. Catal. 244 (2006) 17–23.
[38] S. Li, A. Li, S. Krishnamoorthy, E. Iglesia, Catal. Lett. 77 (2001) 197–205.
[39] T. Fujitani, J. Nakamura, Catal. Lett. 56 (1998) 119–124.
[40] U. Koch, A. Fojtik, H. Weller, A. Henglein, Chem. Phys. Lett. 122 (1985) 507–510.
[41] S.Y. Kim, Y.S. Yeon, S.M. Park, J.H. Kim, J.K. Song, Chem. Phys. Lett. 462 (2008) 100–103.
[42] C.A.K. Gouv a, F. Wypych, S.G. Moraes, N. Dur n, N. Nagata, P. Peralta-Zamora, Chemosphere 40 (2000) 433–440.
[43] S. Su, S.X. Lu, W.G. Xu, Mater. Res. Bull. 43 (2008) 2172–2178.
[44] P.E. Strizhak, O.Z. Didenko, G.R. Kosmambetova, Mater. Lett. 62 (2008) 4094–4096.
[45] R.M. Rioux, R. Komor, H. Song, J.D. Hoefelmeyer, M. Grass, K. Niesz, P. Yang, G.A. Somorjai, J. Catal. 254 (2008) 1–11.
[46] P. Amigues, S.J. Teichner, Discuss. Faraday Soc. 41 (1966) 362–379.
[47] S.F. Jen, A.B. Anderson, Surf. Sci. 223 (1989) 119–130.
[48] D.W. Bahnemann, Isr. J. Chem. 33 (1993) 115–136.
[49] D.W. Bahnemann, C. Kormann, M.R. Hoffmann, J. Phys. Chem. 91 (1987) 3789–3798.
[50] Z. Hu, G. Oskam, P.C. Searson, J. Colloid Interface Sci. 263 (2003) 454–460.
[51] Z. Hu, G. Oskam, R.L. Penn, N. Pesika, P.C. Searson, J. Phys. Chem. B 107 (2003) 3124–3130.
[52] N. Toshima, T. Yonezawa, New J. Chem. 22 (1998) 1179–1201.
[53] L.I. Berger, Semiconductor Materials, CRC Press, New York, 1997.
[54] L.E. Brus, J. Chem. Phys. 80 (1984) 4403–4409.
[55] U. Kreibig, M. Vollmer, Optical Properties of Metal Clusters. Springer Series in Materials Science 25, Springer, Berlin, Heidelberg, 1995.
[56] N.S. Pesika, K.J. Stebe, P.C. Searson, J. Phys. Chem. B 107 (2003) 10412–10415.
[57] G. Kortum, W. Braun, G. Herzog, Angew. Chem. Int. Ed. 2 (1963) 333–404.
[58] K. Klier, Cat. Rev. Sci. Eng. 1 (1968) 207–232.
[59] Y.Y. Tay, S. Li, C.Q. Sun, P. Chen, Appl. Phys. Lett. 88 (2006) 173118.
[60] V.P. Zhdanov, B. Kasemo, Surf. Sci. Rep. 39 (2000) 25–104.
[61] M. Boudart, Chem. Rev. 95 (1995) 661–666.
[62] V.P. Zhdanov, B. Kasemo, Catal. Lett. 50 (1998) 131–134.
[63] E.A. Meulenkamp, J. Phys. Chem. B 102 (1998) 5566–5572.